Studies on the Bi[subscript 2]Te[subscript 3]–Bi[subscript 2]Se[subscript 3]–Bi[subscript 2]S[subscript 3] system for mid-temperature thermoelectric energy conversion

Massachusetts Institute of Technology

Studies on Bi$_2$Te$_3$-Bi$_2$Se$_3$-Bi$_2$S$_3$ System for Mid-Temperature Thermoelectric Energy Conversion

Weishu Liu,[a] Kevin Lukas,[a] Kenneth McEnaney,[b] Sangyeop Lee,[b] Qian Zhang,[a] Cyril Opeil1,[a] Gang Chen *[b] and Zhifeng Ren*[a]

5

[a] Department of Physics, Boston College, Chestnut Hill, Massachusetts 02467, USA. Fax: 1-617-552-8478; Tel: 1-617-552-2832; E-mail: renzh@bc.edu
[b]Department of Mechanical Engineering, Massachusetts Institute of Technology, Cambridge, Massachusetts 02139, USA. Fax: 1-617-324-5519; Tel: 1-617-253-0006; E-mail: gchen2@mit.edu
10 * To whom correspondence should be addressed: gchen2@mit.edu; renzh@bc.edu

Bismuth telluride (Bi$_2$Te$_3$) and its alloys have been widely investigated as thermoelectric materials for cooling applications at around room temperature. We report a systematic study on many compounds in the Bi$_2$Te$_3$-Bi$_2$Se$_3$-Bi$_2$S$_3$ system. All the samples were fabricated 15 by high energy ball milling followed with hot pressing. Among the investigated compounds, Bi$_2$Te$_2$S$_1$ shows a peak ZT ~0.8 at 300 $^{\circ}$C and Bi$_2$Se$_1$S$_2$ ~0.8 at 500 $^{\circ}$C. These results show that these compounds can be used for mid-temperature power generation applications. The leg efficiency of thermoelectric conversion for segmented elements based on these n-type materials could potentially reach 12.5% with cold side at 25 $^{\circ}$C and hot side at 500 $^{\circ}$C if appropriate p-type legs are paired, which could compete well with the state-of-the-art n-type materials within the same temperature range, including lead tellurides, lead selenides, lead sulfides, filled-skutterudites, and half 20 Heuslers.

Broader Context

Thermoelectric convertor has provided a new class of green energy from solar heat, terrestrial heat, waste heat from both automobile vehicles and industrial operations. Bi$_2$Te$_3$-based materials have distinguished themself in low-temperature power generation applications. 25 For these applications, the hot side temperature is typically limited to less than 250 $^{\circ}$C due to the declining ZT value. For the mid-temperature range, PbTe and skutterudite materials were being considered as the candidates. However, the toxicity or thermal stability issue is still the most worrying part for these materials. In this work, we proposed an alternative way by using a segmented leg made from Bi$_2$(Te, Se, S)$_3$-based materials, which shows a potential leg efficiency of 12.5% with cold side of 25 $^{\circ}$C and hot side of 500 $^{\circ}$C. It competes well with the state-of-the-art n-type materials within the same temperature range. Specifically, two new compounds, *i.e.,* 30 Bi$_2$Te$_2$S$_1$ and Bi$_2$Se$_1$S$_2$, have been identified as the promising materials for the mid-temperature applications.

1. Introduction

Bismuth telluride (Bi$_2$Te$_3$) crystalizes in a rhombohedral lattice ($R\overline{3}m$), and shows a lamella structure with a five atomic layer block in the sequence of Te(1)-Bi-Te(2)-Bi-Te2(1).[1] Bi$_2$Te$_3$ is a good thermoelectric material near room temperature,[2] and has dominated the 35 thermoelectric cooling application. The thermoelectric performance of a material is based on a dimensionless figure of merit, *ZT*, which is defined as $ZT=(S^2\sigma/\kappa)T$, where S, σ, κ, and T are the Seebeck coefficient, electrical conductivity, thermal conductivity, and absolute temperature, respectively. Recently, Bi$_2$Te$_3$-based nanocomposites synthesized from powder metallurgy method draw more attentions as a result of their better thermoelectric and mechanical properties.[3 -12] Bi$_2$Te$_3$-based materials are also used in low-temperature heat to electricity conversion applications, including solar to electrical generation.[13,14] For these applications, the hot side temperature is typically 40 less than 250 $^{\circ}$C due to the *ZT* value drop and materials' instability above 300 $^{\circ}$C. For the mid-temperature range between 200-600 $^{\circ}$C, other materials such as PbTe, skutterudites, and half Heuslers are being studied. The primary motivation of this work is to explore some new compositions within the Bi$_2$Te$_3$-Bi$_2$Se$_3$-Bi$_2$S$_3$ system to achieve higher *ZT* values in the mid-temperature range.

Historically, partial substitution of tellurium in Bi$_2$Te$_3$ by selenium (Se) or sulfur (S) was used to reduce the lattice thermal conductivity thereby raising the *ZT* value in n-type Bi$_2$Te$_3$-based thermoelectric materials.[2, 15-18] Bi$_2$Se$_3$ and Bi$_2$S$_3$ were much less studied as 45 thermoelectric materials than Bi$_2$Te$_3$.[19-22] Recently, Biswas *et al.* reported that a *ZT* value of 0.6 at 487 $^{\circ}$C was obtained in an n-type Bi$_2$S$_3$ ingot doped with BiCl$_3$.[23] The peak *ZT* value of such Te-free thermoelectric material is still low as compared with Bi$_2$Te$_3$, but Bi$_2$Te$_3$ is not stable above 300 $^{\circ}$C. In this report, we investigate the thermoelectric properties of some new compositions in Bi$_2$Te$_3$-Bi$_2$Se$_3$-Bi$_2$S$_3$

system to see whether these materials can be used at temperatures higher than 300 ^{o}C. According to our study, the peak *ZT* of Bi$_2$Te$_{2.7}$Se$_{0.3}$ shifted from 125 ^{o}C to 200 ^{o}C by partially substituting Te with S, also a peak *ZT* of ~0.8 at 300 ^{o}C could be obtained in Bi$_2$Te$_2$S$_1$ and ~0.8 at 500 ^{o}C in Bi$_2$Se$_1$S$_2$ by carrier concentration optimization. These results place such materials as promising candidates for intermediate temperature (300-500 ^{o}C) thermoelectric applications.

2. Experimental details

Synthesis. The fabrication process is similar to that of our previous reports.[11, 12] Bismuth chunks (Bi, 99.999%, Alfa Aesar), tellurium chunks (Te, 99.999%, Alfa Aesar), selenium shots (Se, 99.999%, Alfa Aesar), and sulfur powders (S, 99.99%, Alfa Aesar) were weighted according to the stoichiometric Bi$_2$(Te, Se, S)$_3$, specified in each section, plus a very tiny amount of copper for either process repeatability control or carrier concentration adjustment (the exact amount for each composition will be described in the appropriate places). The elements were then subjected to ball milling for 20 hours. The ball milled powders were then loaded into a graphite die with an inner diameter of 12.7 mm and sintered by direct current induced hot pressing (dc-HP) at 500 ^{o}C for 2 minutes into a rod with a height of 12-13 mm. These dimensions allow us to carry out the thermal and electrical conductivity measurements along the same direction (all the data reported in this paper are from the same direction).

Crystalline structure. X-ray diffraction measurements were conducted on a PANalytical multipurpose diffractometer with an X'celerator detector (PANalytical X'Pert Pro). The lattice parameters and atomic sites of each element in the Bi$_2$(Te, Se, S)$_3$ phase were calculated by the Rietveld refinement method, which was performed using a commercial software (X'Pert High Score Plus, X'Pert Pro).

Thermoelectric transport properties. The electrical resistivity was measured by a reversed dc-current four-point method, while the Seebeck coefficient was determined by the slope of the voltage difference versus temperature difference curve based on a static temperature difference method. The simultaneous measurement of electrical resistivity and Seebeck coefficient was conducted on a commercial system (ZEM-3, ULVAC). The thermal conductivity was calculated from the relationship $\kappa=DC_pd$, where D, C_p, and d are the thermal diffusivity, specific heat, and volumetric density, respectively. The thermal diffusivity was measured by the laser flash method with a commercial system (LFA447, Netzsch). The specific heat capacity was determined by two differential scanning calorimeters (DSC200-F3 for the C_p from 25 to 250 ^{o}C, DSC404-C for the C_p from 250 to 500 ^{o}C Netzsch). The volumetric density (listed in Table 1) was measured by the Archimedes method. The Hall coefficient, R_H, measurement was carried out on two commercial systems (PPMS, Quantum Design; Electromagnet7600, LakeShore), with a magnetic field up to 9T and an electrical current of 10-20 mA.

3. Results and discussion

3.1 Bi$_2$Te$_3$-Bi$_2$Se$_3$-Bi$_2$S$_3$

Fig. 1 shows the phase diagram for the Bi$_2$Te$_3$-Bi$_2$Se$_3$-Bi$_2$S$_3$ system, which includes more than ten nominal compositions studied. Three regions could be identified: rhombohedral region (Bi$_2$Te$_3$, Bi$_2$Te$_2$Se$_1$, Bi$_2$Te$_1$Se$_2$, Bi$_2$Se$_3$, Bi$_2$Te$_2$S$_1$, and Bi$_2$Te$_{1.8}$Se$_{0.6}$S$_{0.6}$, filled circles), orthorhombic region (Bi$_2$S$_3$, Bi$_2$Se$_1$S$_2$, and Bi$_2$Se$_2$S, open circles), and a mixture region (Bi$_2$Te$_1$S$_2$, Bi$_2$Te$_1$Se$_1$S$_1$, Bi$_2$Te$_{0.6}$Se$_{1.8}$S$_{0.6}$, and Bi$_2$Te$_{0.6}$Se$_{0.6}$S$_{1.8}$, half-filled circles). In the Bi$_2$Te$_3$-Bi$_2$Se$_3$ system, the interphases Bi$_2$Te$_2$Se$_1$ (named as Kawazulite) and Bi$_2$Te$_1$Se$_2$ (named as Skippenite) have been early identified in natural mine,[24] but were less intentionally studied as compared with Bi$_2$Te$_3$ and Bi$_2$Se$_3$. The varying lattice parameters (*a*, *b* and *c*) from Bi$_2$Te$_3$ to Bi$_2$Se$_3$ follow the Vegard's law, which indicates a linear structure shrinkage. The detailed lattice parameters and atomic sites are given in Table 1. Liu *et al.* reported a miscibility gap between the rhombohedral phase Bi$_2$Se$_3$ and orthorhombic phase Bi$_2$Se$_2$S$_1$ in the Bi$_2$Se$_3$-Bi$_2$S$_3$ system.[25] A similar miscibility gap has also been observed in our work. The sulfur-rich phases Bi$_2$Se$_1$S$_2$ and Bi$_2$Te$_1$S$_2$ were not well studied in literature. According to our study, Bi$_2$Se$_1$S$_2$ is a single phase and shares a similar crystalline structure with Bi$_2$S$_3$. In the crystalline structure of Bi$_2$S$_3$, sulfur has three equivalent sites S(1) (0.6154, 0.75, 0.0576), S(2) (0.7148, 0.25, 0.3055), and S(3) (0.4505, 0.75, 0.3609). The crystalline structure information of Bi$_2$S$_3$ was used as the starting value for the Rietveld refinement of the Bi$_2$Se$_1$S$_2$ XRD pattern. All three possible substitutions of sulfur with selenium have been investigated. Se atoms in the Bi$_2$Se$_1$S$_2$ compound are most likely in the S(2)-site of the Bi$_2$S$_3$-type lattice structure, as shown in Table 1. Bi$_2$Te$_1$S$_2$ is a mixture of a rhombohedral phase (63.2 mol.%) and an orthorhombic phase (36.8 mol.%), which indicates another miscibility gap between Bi$_2$S$_3$ and Bi$_2$Te$_2$S$_1$. Additionally, the nominal compositions Bi$_2$Te$_1$Se$_1$S$_1$, Bi$_2$Te$_{0.6}$Se$_{1.8}$S$_{0.6}$, and Bi$_2$Te$_{0.6}$Se$_{0.6}$S$_{1.8}$ are also a mixture of the rhombohedral and orthorhombic phase. The predicted mixture region, presented in Fig. 1 by the shaded region, is useful to design new nanostructures to achieve a reduced lattice thermal conductivity by controlling the size, morphology, and concentration of the precipitation phase.[26, 27]
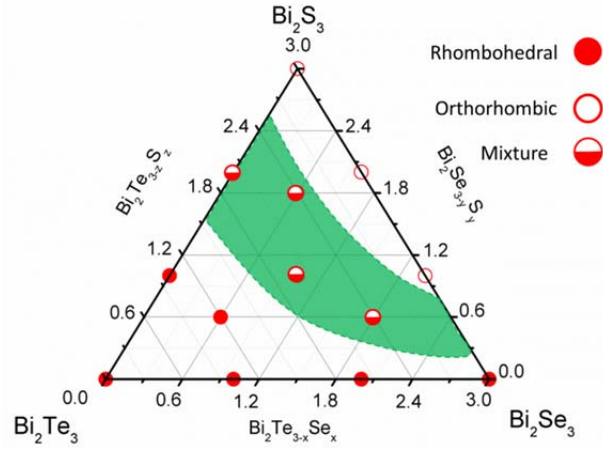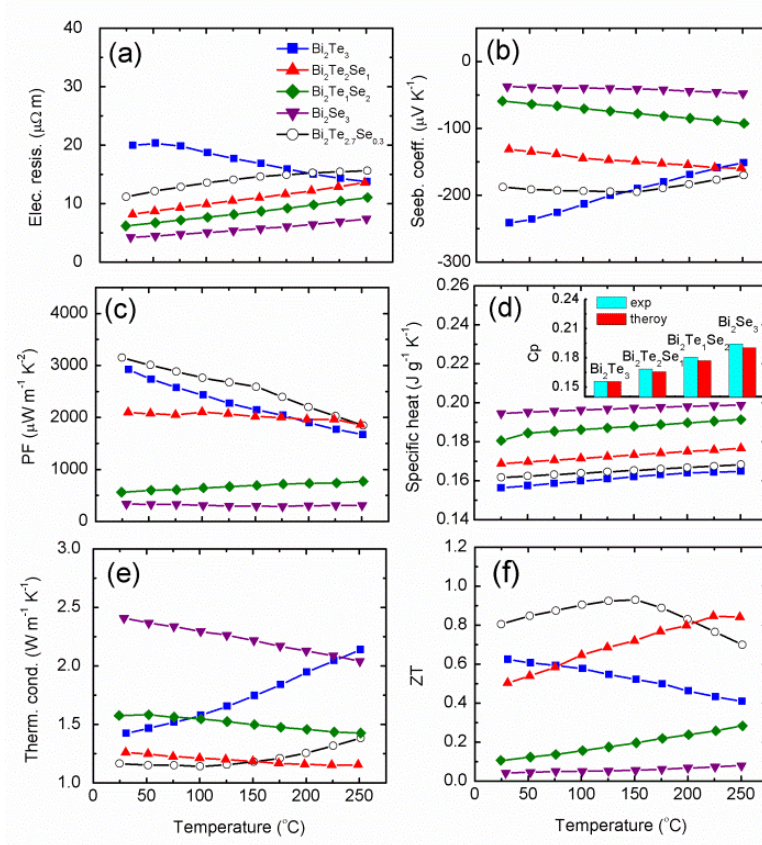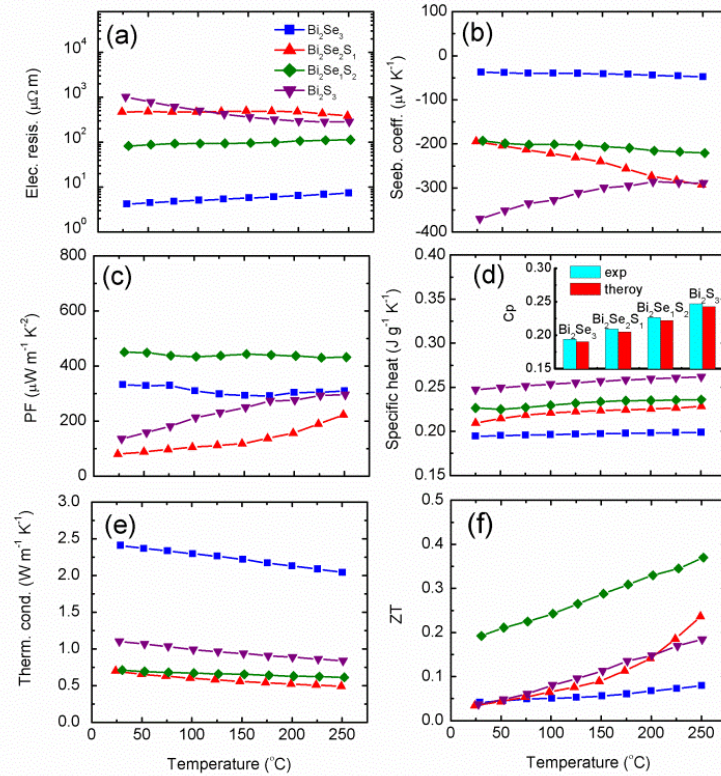
Fig. 1. Phase diagram of Bi_2Te_3-Bi_2Se_3-Bi_2S_3 system.

Fig. 2, Temperature dependent thermoelectric properties of the Bi_2Te_3-Bi_2Se_3 system, (a) electrical resistivity, (b) Seebeck coefficient, (c) power factor, (d) specific heat, (e) thermal conductivity, (f) figure of merit ZT. The inset of figure (d) shows the comparison of specific heat at room temperature between the experimentally measured value and theoretically calculated value.

Fig. 2 shows the temperature dependent thermoelectric properties of the Bi_2Te_3-Bi_2Se_3 system. In order to achieve good process repeatability, 1 at.% copper (Cu) was used.[12] Fig. 2(a) demonstrates a continuous decrease in electrical resistivity with increasing Se content from Bi_2Te_3 to Bi_2Se_3. The negative sign of the Seebeck coefficient for all these samples indicates n-type carriers, as shown in Fig. 2(b). The Seebeck coefficient at room temperature dramatically decreases from -241, to -131, -59 and -37 μV K^{-1} for the samples of

3

Bi$_2$Te$_3$, Bi$_2$Te$_2$Se$_1$, Bi$_2$Te$_1$Se$_2$, and Bi$_2$Se$_3$, respectively, which is in agreement with the trend observed in electrical resistivity. The considerable changes in both the electrical resistivity and Seebeck coefficient suggest a rising carrier concentration or band structure change with the increased Se in the Bi$_2$Te$_{3-x}$Se$_x$ system. A possible explanation is that Se has higher evaporation pressure than Te and hence easily forms donor-like vacancies in the Bi$_2$Te$_3$-type lattice.[28] Owing to the large difference in Seebeck coefficient, the Bi$_2$Se$_3$ sample has a much lower power factor (330 μW m^{-1} K^{-2}) than Bi$_2$Te$_3$ sample (2920 μW m^{-1} K^{-2}), as shown in the Fig. 2(c). Fig. 2(d) shows the measured specific heat for these samples, which are 2~8% higher than the theoretical value from Dulong–Petit law, depending on the temperatures. The inset of Fig. 2(d) compares the difference in specific heat for the Bi$_2$Te$_{3-x}$Se$_x$ system between measured values and theoretical values at room temperature. The thermal conductivities are plotted in Fig. 2(e), from which we can see that Bi$_2$Se$_3$ has the highest thermal conductivity associated with the large contribution from the electrons. In order to confirm the impact of alloying effect on the phonon transport, the lattice thermal conductivities at room temperature are estimated from $\kappa_{lat}=\kappa_{tot}-L\sigma T$, where the Lorenz numbers (L) are calculated by using the Fermi energies derived from Seebeck coefficients.[12] The lattice thermal conductivities of Bi$_2$Te$_{3-x}$Se$_x$ system are 1.18, 0.73, 0.60, 0.47, and 0.66 W m^{-1} K^{-1}, for x=0, 0.3, 1, 2 and 3, respectively. A valley in the lattice thermal conductivity was clearly seen in Bi$_2$Te$_3$-Bi$_2$Se$_3$ system. This phenomenon could be understood through the effect of imperfections on the heat transport by lattice in a solid solution. The mass fluctuation and chemical bond changing were believed to generate strong scattering to the transport of phonons. [29, 30] Due to the high power factor and low thermal conductivity, the classic composition Bi$_2$Te$_{2.7}$Se$_{0.3}$ shows the highest peak *ZT* value, *i.e.*, ~0.9 at 150 ^{o}C. Additionally, the Bi$_2$Te$_2$Se$_1$ sample shows a *ZT* value of ~0.8 at 250 ^{o}C, which is good for thermoelectric applications at temperatures higher than 200 ^{o}C.

Fig.3. Temperature dependent thermoelectric properties of the Bi$_2$Se$_3$-Bi$_2$S$_3$ system, (a) electrical resistivity, (b) Seebeck coefficient, (c) power factor, (d) specific heat, (e) thermal conductivity, (f) figure of merit ZT. The inset of figure (d) shows the comparison of specific heat at room temperature between the experimentally measured value and theoretically calculated value.
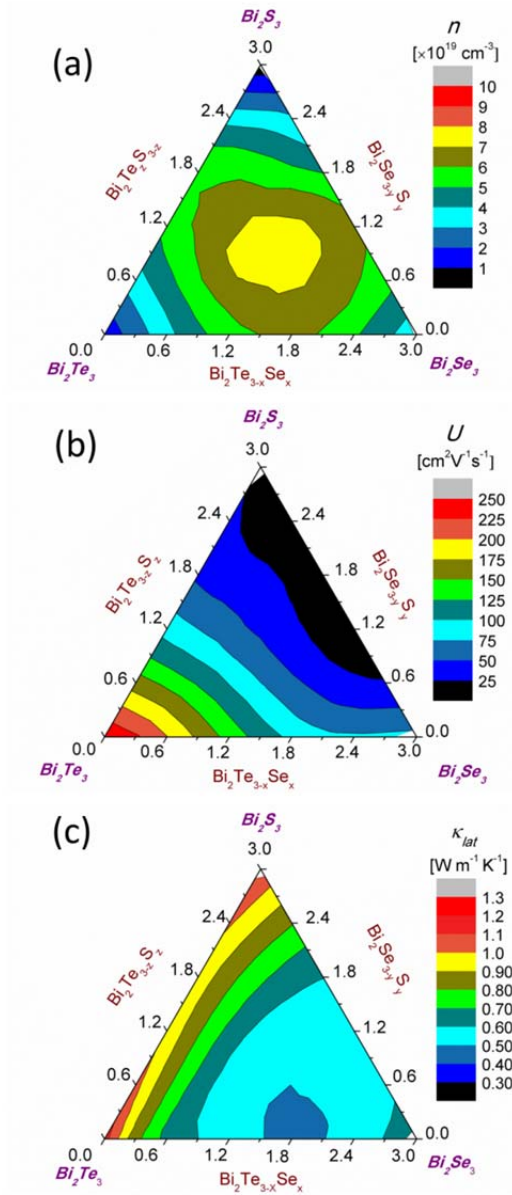
In contrast to the Bi$_2$Te$_3$-Bi$_2$Se$_3$ system, the Bi$_2$Se$_3$-Bi$_2$S$_3$ system shows a totally different picture owing to the lattice structure difference between Bi$_2$Se$_3$ and other S-containing Bi$_2$Se$_{3-y}$S$_y$ compounds, as indicated in the Fig. 3. Here, a similar amount of Cu (1 at.%) was used for achieving good process repeatability. The rhombohedral phase (Bi$_2$Se$_3$) shows heavily doped n-type semiconducting behavior, *i.e.*, low electrical resistivity (4.2 μΩ m at 25 ^{o}C) and Seebeck coefficient (-37 μV K^{-1} at 25 ^{o}C). However, all the investigated orthorhombic phases show very poor electrical conductivity, resulting from a lower carrier concentration than Bi$_2$Se$_3$. From the electrical resistivity and Seebeck coefficient plotted in Fig. 3(a) and (b), no obvious trend connected with the sulfur content can be identified within the

orthorhombic phase region. Among the three orthorhombic phases, the power factor 430 μW m^{-1} K^{-2} of Bi$_2$Se$_1$S$_2$ is slightly higher than 295 μW m^{-1} K^{-2} of Bi$_2$S$_3$ and 220 μW m^{-1} K^{-2} of Bi$_2$Se$_2$S$_1$ at 250 $^\circ$C, as shown the Fig. 3(c). The power factor of the as-pressed Bi$_2$S$_3$ is slightly higher than that of Bi$_2$S$_{3-\delta}$ made by a similar powder metallurgy process.[20] The thermal conductivities, calculated by using the measured specific heat and diffusivity coefficient, are plotted in the Fig. 3(e). All the samples show almost a linear decrease with increasing temperature, without notable bipolar effect. Because of the low power factor, the *ZT* values of Bi$_2$Se$_3$ and Bi$_2$S$_3$ are only 0.05 near room temperature and 0.1~0.2 at 250 $^\circ$C. However, the *ZT* values of both Bi$_2$Se$_1$S$_2$ and Bi$_2$Se$_2$S$_1$ rise with temperature, demonstrating a potential high temperature application. (The high temperature, up to 500 $^\circ$C, thermoelectric properties of Bi$_2$Se$_1$S$_2$ are also measured and are shown in Fig. 7)
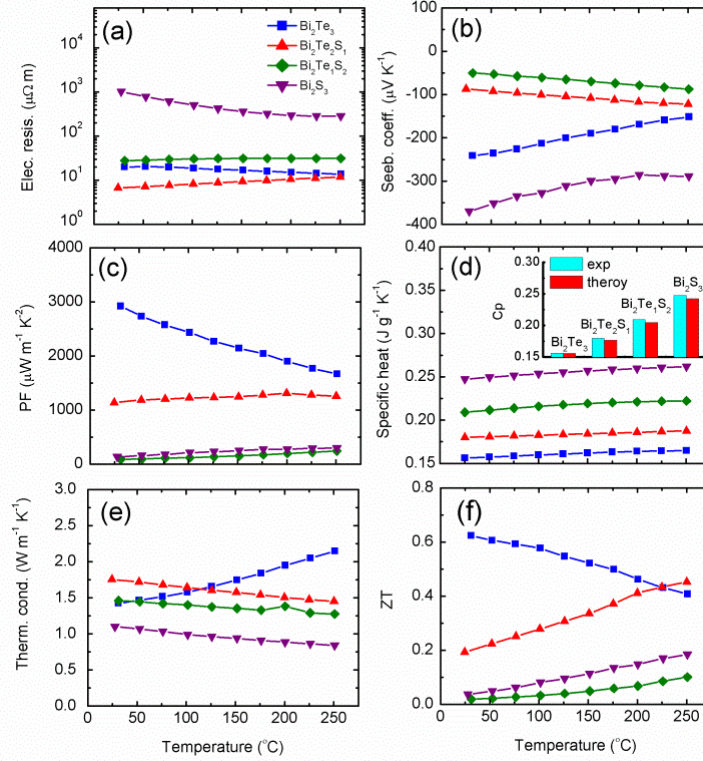
Fig.4. Temperature dependent thermoelectric properties of the Bi$_2$Te$_3$-Bi$_2$S$_3$ system, (a) electrical resistivity, (b) Seebeck coefficient, (c) power factor, (d) specific heat, (e) thermal conductivity, (f) figure of merit ZT. The inset of figure (d) shows the comparison of specific heat at room temperature between the experimentally measured value and theoretically calculated value.

Fig. 4 shows the thermoelectric properties of the Bi$_2$Te$_3$-Bi$_2$S$_3$ system with 1 at.% Cu for achieving good process repeatability. In contrast to Bi$_2$Se$_{3-y}$S$_y$, the solution limit of sulfur in Bi$_2$Te$_{3-z}$S$_z$ is much higher. In the rhombohedral phase region, both the electrical resistivity and Seebeck coefficient of Bi$_2$Te$_{3-z}$S$_z$ decrease significantly with increasing sulfur content, as shown in Fig. 4(a) and (b). Here, sulfur behaves as a strong donor in Bi$_2$Te$_{3-z}$S$_z$, which is similar to the effect of Se in Bi$_2$Te$_{3-x}$Se$_x$. A similar donor behavior for sulfur was also identified in Bi$_2$Te$_{3-z}$S$_z$ ingot.[31] The calculated lattice thermal conductivities near room temperature are 1.18, 0.89, 0.97, and 1.10 W m^{-1} K^{-1} for Bi$_2$Te$_3$, Bi$_2$Te$_2$S$_1$, Bi$_2$Te$_1$S$_2$, and Bi$_2$S$_3$, respectively. Due to the narrow band gap, the *ZT* value of Bi$_2$Te$_3$ shows a large decrease from 0.62 to 0.41 with increasing temperature from 25 to 250 $^\circ$C. In contrast, Bi$_2$Te$_2$S$_1$ shows a continuous rise from 0.2 to 0.45, suggesting that Bi$_2$Te$_2$S$_1$ could be a new candidate for higher temperature application after further carrier optimization.

Fig. 5, (a) Hall carrier concentration, (b) weighted mobility, and (c) lattice thermal conductivity of the Bi_2Te_3-Bi_2Se_3-Bi_2S_3 system.

In order to fully show the Bi_2Te_3-Bi_2Se_3-Bi_2S_3 system, contouring diagrams were plotted in Fig. 5 according to the Hall carrier concentration, weighted mobility, and lattice thermal conductivity at room temperature. Here, the Hall carrier concentration is calculated by using the relationship of $n_H = 1/(eR_H)$, where e and R_H are free charge and Hall coefficient, respectively, as shown in the Fig. 5(a). At first glance, a mountain of carrier concentration n_H is shown near the center of the Bi_2Te_3-Bi_2Se_3-Bi_2S_3 diagram. It is consistent with our observation that $Bi_2Te_1Se_1S_1$ has much low electrical resistivity (6.2 µΩ m at 25 °C) and Seebeck coefficient (-31.5 µV K^{-1} at 25 °C). Another feature is that the carrier concentration of the composition at the edge is higher than that of the compositions at the corners (*i.e.*, Bi_2Te_3, Bi_2Se_3, and Bi_2S_3). Generally, the increased carrier concentration with the substitution of Te in Bi_2Te_3 by Se or S is resulted from the increased vacancy at the Te-site of the Bi_2Te_3 lattice. Fig. 5(a) shows a similar trend at the Bi_2Te_3-rich end. The measured electrical resistivity and Seebeck coefficient, plotted in Fig. 2 and Fig. 4, also demonstrate a similar trend. The n_H of Bi_2Se_3 is much higher than Bi_2Te_3, and slightly lower than that of $Bi_2Te_2Se_1$ and Bi_2TeSe_2.

According to previous theoretical studies,[32,33] the combination of the carrier mobility and effective mass, *i.e.*, $\mu(m^*/m_0)^{3/2}$, can be an index to determine whether a material is good for the thermoelectric purpose. According to Slack's definition,[34] the parameter $\mu(m^*/m_0)^{3/2}$ is

6

named as weighted carrier mobility U, where μ, m^*, and m_0 are the carrier mobility, the density of states effective mass for the conduction band (or valence band), and the free electron mass, respectively. Generally, a material with heavy m^* usually has low μ. A high value of U usually means a high power factor PF ($PF=S^2\sigma$) at an optimized carrier concentration. Fig. 5(b) plots the weighted carrier mobility for the Bi_2Te_3-Bi_2Se_3-Bi_2S_3 system. Here, the values of U were deduced from the measured Seebeck coefficient and electrical conductivity according to the following equations, [35]

$$S = -\frac{k_B}{e}\left(\frac{(r+5/2)F_{r+3/2}(\xi)}{(r+3/2)F_{r+1/2}(\xi)} - \xi\right), \tag{1}$$

$$\sigma = 2e\left(\frac{2\pi m_0 k_B T}{h^2}\right)^{3/2}\left(m^*/m_0\right)^{3/2}\mu F_{r+1/2}(\xi), \tag{2}$$

$$F_n(\xi) = \int_0^\infty \frac{x^n}{1+e^{(x-\xi)}}dx, \tag{3}$$

where the e, r, k_B, and h are the free electron charge, scattering parameter, Boltzman constant, and Plank constant, respectively. The numerical calculation process of U is, 1) to get the reduced Fermi energy ξ from Equation(1), 2) to insert ξ into Equation (2) to get $\mu(m^*/m_0)_{3/2}$, with the measured S and σ, and assumption of acoustic phonon scattering (r=-1/2). From Fig. 5(b), it is clearly shown that Bi_2Te_3 has the highest weighted mobility, while the substitutions of Te with Se or S yield a significant decrease in weighted carrier mobility. This phenomenon is in good agreement with the normal observations that Bi_2Te_3 has a higher power factor than Bi_2Se_3 and Bi_2S_3. Polycrystalline samples made by ball milling and hot pressing could have power factors over 3000 $\mu W\ m^{-1}\ K^{-2}$, about ten times higher than that of Bi_2S_3 even at an optimized carrier concentration.

Fig. 5(c) shows the lattice thermal conductivity for the Bi_2Te_3-Bi_2Se_3-Bi_2S_3 system. Firstly, the decreased lattice thermal conductivities associated with the alloying effect are seen in all the three subsystems, the valley of the lattice thermal conductivity is located at the mixture region of the rhombohedral and orthorhombic phase for both the Bi_2Te_3-Bi_2S_3 and Bi_2Se_3-Bi_2S_3 subsystems. In the Bi_2Te_3-Bi_2Se_3 system, the minimum value is very close to $Bi_2Te_{1.2}Se_{1.8}$. Secondly, the minimum lattice thermal conductivity value in the Bi_2Se_3-Bi_2S_3 system is higher than that in the Bi_2Te_3-Bi_2Se_3 system.

3.2 $Bi_2Te_{2.7-x}Se_{0.3}S_x$

Since Bi_2Te_3 has high lattice thermal conductivity, partial substitution of Te with Se to form a $Bi_2Te_{3-x}Se_x$ alloy is essential to optimize the ZT value. $Bi_2Te_{2.7}Se_{0.3}$ is the classic composition for thermoelectric applications near room temperature. However, the ZT value of $Bi_2Te_{2.7}Se_{0.3}$ drops quickly as the temperature becomes higher than 200 ^oC. We studied the effect of partial replacement of Te with S in the classic composition $Bi_2Te_{2.7}Se_{0.3}$. In these samples, a 0.5 at% Cu was used to achieve good process repeatability. Fig. 6(a-e) shows the temperature dependent thermoelectric properties of as-pressed $Bi_2Te_{2.7-x}Se_{0.3}S_x$ with different sulfur doping concentrations (x=0, 0.2, and 0.4). The Seebeck coefficient of $Bi_2Te_{2.7-x}Se_{0.3}S_x$ roughly decreases with increasing sulfur content at room temperature, demonstrating a donor behavior. The possible reason would be the reduced formation energy of Te-site vacancies as sulfur partially substitutes for tellurium of the Bi_2Te_3-type crystalline structure. Another notable character of the temperature dependent electrical resistivity and Seebeck coefficient, plotted in Fig. 6(a) and (b), is the peak value (ρ_{max} and S_{max}) shifted towards higher temperatures. This change is a typical behavior of a suppressed bipolar effect due to the increasing of extrinsic carrier.[36] Owing to the decreasing weighted mobility with the addition of sulfur, a large decrease of power factor was seen near room temperature in $Bi_2Te_{2.7-x}Se_{0.3}S_x$: from 2401, to 1773, and 1255 $\mu W\ m^{-1}\ K^{-2}$ for x=0, 0.2, and 0.4, respectively. Fig. 6(d) is the temperature dependent thermal conductivity of the as-pressed $Bi_2Te_{2.7-x}Se_{0.3}S_x$. Most noticeable is the less bipolar contribution to the thermal conductivity with increasing sulfur content. It is shown that $Bi_2Te_{2.7}Se_{0.3}$ has a quick rising thermal conductivity as temperature is increased above 150 ^oC, on the contrary, $Bi_2Te_{2.3}Se_{0.3}S_{0.4}$ has a quite slow rise in the whole temperature range from room temperature to 325 ^oC. As a result, the temperature for the peak ZT shifted from 125 ^oC for $Bi_2Te_{2.7}Se_{0.3}$ (ZT_{max} ~0.8) to 200 ^oC for $Bi_2Te_{2.3}Se_{0.3}S_{0.4}$ (ZT_{max} ~0.7), see Fig. 6(e).

It was reported that re-orientation of randomly distributed grains help to achieve a ZT enhancement of n-type Bi_2Te_3-based thermoelectric materials.[9, 11] Here, a twice-repressing process was used to get stronger (00l)-texture, in contrast to the previous once-repressing process, and finally higher ZT along the direction perpendicular to the press direction. Fig. 6 (f-j) shows the temperature dependent thermoelectric properties of the twice-repressed $Bi_2Te_{2.7-x}Se_{0.3}S_x$ with different amount of sulfur concentrations (x=0, 0.2, and 0.4). As compared with the as-pressed sample, the twice-repressed sample shows a considerable reduction in electrical resistivity due to texturing. Additionally, a slight decrease in the Seebeck coefficient is observed, which is related to the increase of Te vacancies owing to

the mechanical deformation during the hot pressing process.[12, 37] Benefitting from the enhanced texture, the power factors show significant improvement: from 2401 to 3845 $\mu W \, m^{-1} \, K^{-2}$ for $Bi_2Te_{2.7}Se_{0.3}$ (~60% enhancement) and from 1255 to 2234 $\mu W \, m^{-1} \, K^{-2}$ for $Bi_2Te_{2.3}Se_{0.3}S_{0.4}$ (~78 % enhancement). It is worth pointing out that the highest power factor we obtained previously by only once-repressing is about 3390 $\mu W \, m^{-1} \, K^{-2}$. The thermal conductivity of the twice-repressed sample is obviously higher than the as-pressed sample because of the larger contribution from the carriers, as shown in Fig. 6(d) and (i). Even with the higher thermal conductivity, the ZT values of all the twice-repressed $Bi_2Te_{2.7-x}Se_{0.3}S_x$ samples are still much higher than that of the as-pressed samples. As examples, the enhancement of the peak ZT value for $Bi_2Te_{2.3}Se_{0.3}S_{0.4}$ is ~14% from ~0.7 (as-pressed) to ~0.8 (twice-repressed). Similarly, $Bi_2Te_{2.7}Se_{0.3}$ shows an even larger enhancement of ~38% from ~0.8 (as-pressed) to ~1.1 (twice-repressed). Furthermore, the temperature dependent ZT curve for $Bi_2Te_{2.3}Se_{0.3}S_{0.4}$ in the range from 200 to 325 ^{o}C is quite flat with an average value larger than 0.7, which could be a candidate to push the hot side temperature of the current STEG from ~200 ^{o}C to ~325 ^{o}C.
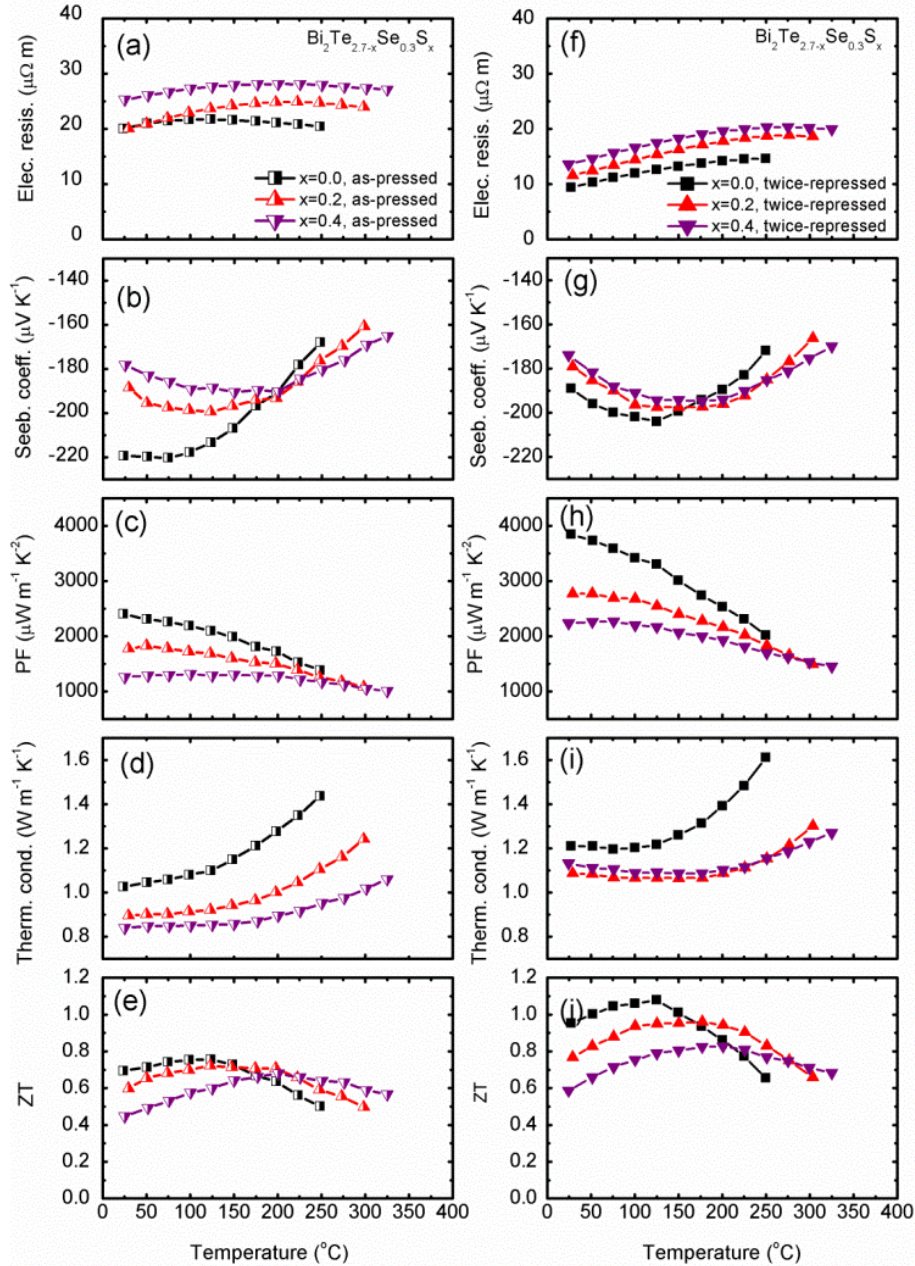
Fig. 6, Temperature dependent thermoelectric properties of the as-pressed and twice-repressed $Bi_2Te_{2.7-x}Se_{0.3}S_x$ with different sulfur content (x=0, 0.2, and 0.4).

3.3 Bi$_2$Se$_1$S$_2$ and Bi$_2$Te$_2$S$_1$

Goldsmid has developed a simple formula to estimate the band gap of a semiconductor from the peak Seebeck coefficient and corresponding temperature, *i.e.*, E_G=2e$S_{max}T$.[38] This simple relationship is applied to the Bi$_2$Te$_3$-Bi$_2$Se$_3$-Bi$_2$S$_3$ system. The band-gap (E_G) enlargement was observed from Bi$_2$Te$_3$, to Bi$_2$Se$_3$, and to Bi$_2$S$_3$. Bi$_2$Te$_2$S$_1$ (E_G=0.20 eV) and Bi$_2$Se$_1$S$_2$ (E_G=0.34 eV) show promising thermoelectric applications at temperatures up to 300-500 °C.
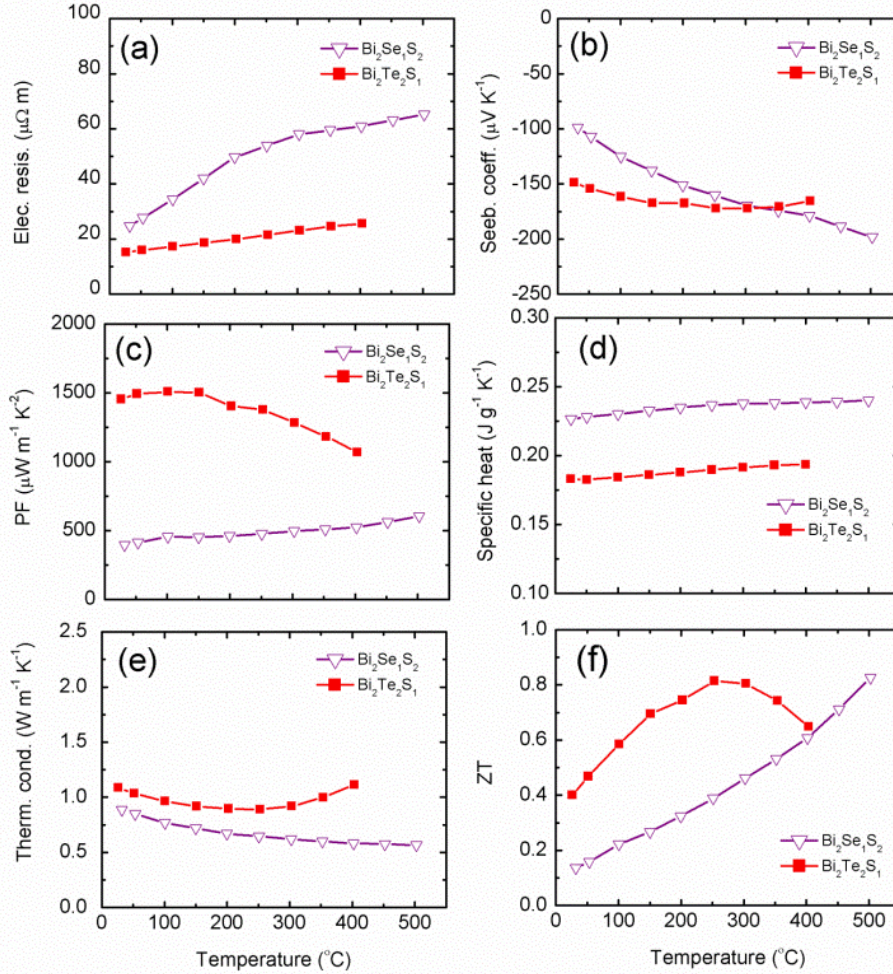
Fig. 7, Temperature dependent thermoelectric properties of the Bi$_2$Se$_1$S$_2$ and Bi$_2$Te$_2$S$_1$.

Fig. 7 shows the temperature dependent thermoelectric properties of these two new compounds: Bi$_2$Se$_1$S$_2$ and Bi$_2$Te$_2$S$_1$. Here 0.05~3 at.% Cu is used to optimize the carrier concentration. For Bi$_2$Se$_1$S$_2$, the increased electrical resistivity and Seebeck coefficient with temperature suggests a behavior of heavily doped semiconductor. Furthermore, a power factor of 603 μW m^{-1} K^{-2} at 500 °C is obtained in Bi$_2$Se$_1$S$_2$, which nearly doubles as compared with the optimized Bi$_2$S$_3$ made by similar powder metallurgy method. The thermal conductivity of Bi$_2$Se$_1$S$_2$ continuously decreases with increasing temperature without any notable bipolar effect. The larger band gap of Bi$_2$Se$_1$S$_2$, as compared with Bi$_2$Te$_3$, is the direct reason for the negligible bipolar thermal conductivity. Benefited from the enlarged band gap, the heavily doped Bi$_2$Se$_1$S$_2$ shows a continuous increase in *ZT* value with increasing temperature from room temperature to 500 °C. A value of ~0.8 at 500 °C is obtained in this Te-free Bi$_2$Se$_1$S$_2$ sample, which corresponds to ~33% enhancement over a reported Bi$_2$S$_3$ ingot.[23] This value makes Bi$_2$Se$_1$S$_2$ competitive with PbS[39] and half-Heusler[40]. Another compound, Bi$_2$Te$_2$S$_1$, has a much higher power factor than that of Bi$_2$Se$_1$S$_2$ because of its higher weighted mobility (as shown in Fig. 5(b)). Bi$_2$Te$_2$S$_1$ shows a peak *ZT* ~0.8 near 300 °C, which indicates its promise to fill the temperature gap for power generation between Bi$_2$Te$_3$ and Bi$_2$Se$_1$S$_2$.

9

3.4 Power generation efficiency of segmented legs

For an ideal thermoelectric converter with constant material properties, the leg efficiency from thermal to electric power (η_{te}) is governed by the Carnot efficiency and a ZT related factor through a relationship,[38]

$$\eta_{te} = \frac{T_h - T_c}{T_h} \left(\frac{\sqrt{1+Z\overline{T}}-1}{\sqrt{1+Z\overline{T}}+\frac{T_c}{T_h}} \right), \qquad (4)$$

where T_h and T_c are the temperatures of hot side and cold side, respectively, $\overline{T}$ is the average temperature between T_h and T_c. When the temperature-dependent properties are considered, $Z\overline{T}$ in equation (4) can be replaced by the average ZT over the whole temperature range from T_c to T_h to provide an estimate of the leg efficiency. Two more accurate methods for calculating the efficiency of a leg with temperature-dependent material properties have been described by Snyder and Ursell,[41] and by Mahan[42]. In this study the discretization method of Mahan is used. The heat flow in the leg is assumed to be one-dimensional, and losses from the sidewalls of the leg are neglected such that Mahan's discretization equations are used, as well as the corresponding discretization for the voltage in the leg:

$$\frac{dT}{dx} = \frac{JST - q}{k} \qquad , \qquad (5)$$

$$\frac{dq}{dx} = \rho J^2 + JS\frac{dT}{dx} \qquad , \qquad (6)$$

$$\frac{dV}{dx} = -\rho J - S\frac{dT}{dx} \qquad , \qquad (7)$$

where J is the current density, q is the heat flux density, ρ is the electrical resistivity, and V is the voltage, S is the Seebeck coefficient, T is the temperature. These equations are solved iteratively to match the temperature boundary conditions at a given current density, J. The efficiency is calculated as the electrical power out divided by the heat flux into the leg:

$$\eta_{leg} = \frac{J(V_c - V_h)}{q_h} \qquad . \qquad (8)$$

The current density is then optimized to maximize the efficiency of the leg.

The best material presented in this paper for high-temperature applications is $Bi_2Se_1S_2$. When the performance of this leg between two heat reservoirs at 500 °C and 25 °C is calculated (via Mahan's method), the efficiency is 7.1%. One of the reasons the efficiency is low because of the low ZT at lower temperatures. However, other materials in this paper have ZTs greater than that of $Bi_2Se_1S_2$ over various portions of the aforementioned temperature range. Therefore an interesting solution would be to use a segmented leg. The segmented leg, shown in Fig. 8(a), comprises the following segments: $Bi_2Te_{2.7}Se_{0.3}$ for 25-175 ^{o}C, $Bi_2Te_{2.5}Se_{0.3}S_{0.2}$ for 175-250 ^{o}C, $Bi_2Te_2S_1$ for 250-400 ^{o}C, and $Bi_2Se_1S_2$ for 400-500 ^{o}C. When such segments are used, the efficiency of the leg is 12.5%. The wide variety of material properties that exist within the Bi_2Te_3-Bi_2Se_3-Bi_2S_3 system provide opportunities for high-efficiency thermoelectric energy conversion.
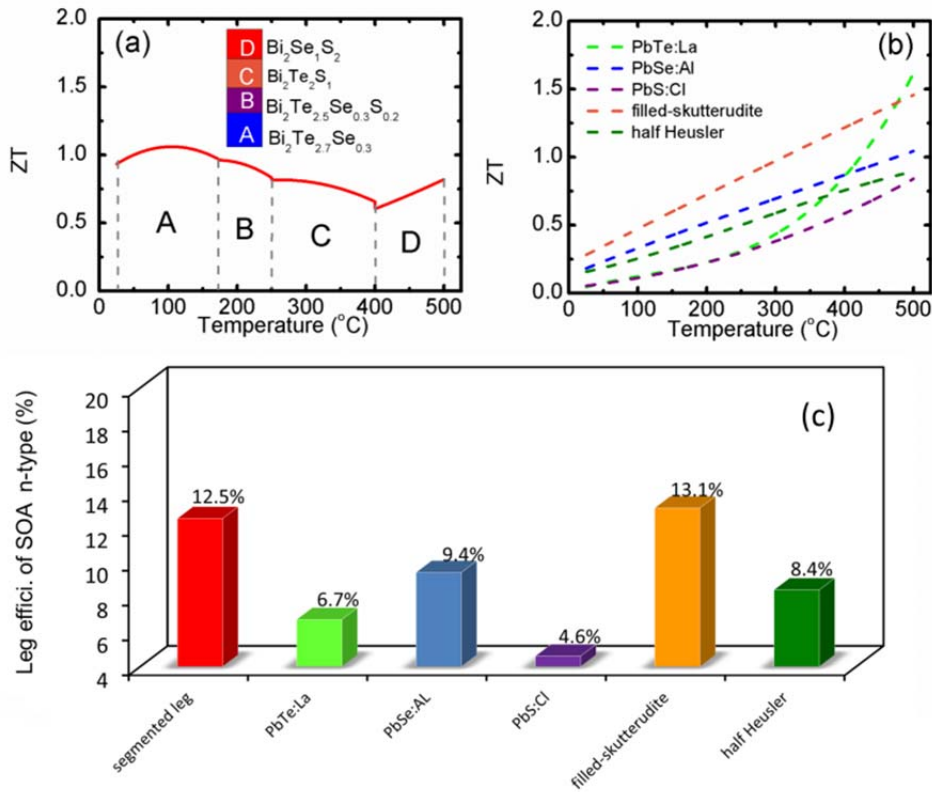
Fig. 8, (a) Temperature dependent *ZT* value of the segmented leg made by the $Bi_2(Te, Se, S)_3$-based materials, (b) temperature dependent *ZT* of the single leg made of the state-of-the-art (SOA) thermoelectric materials, (c) comparison of leg efficiency between the $Bi_2(Te, Se, S)_3$-based segmented leg with SOA single leg with T_c=25 ^{o}C and T_h=500 ^{o}C.

For comparison, the *ZT* values of the state-of-the-art (SOA) thermoelectric materials are also plotted in Fig. 8 (b), which include PbTe:La[43], PbSe:Al[44], PbS:Cl[39], filled-skutterudites[45], and half Heuslers[40]. The 12.5% efficiency of the segmented leg based on Bi_2Te_3-Bi_2Se_3-Bi_2S_3 materials compares well with that of other thermoelectric materials over the same temperature range: PbTe:La (6.7%), PbSe:Al (9.4%), PbS:Cl (4.6%), filled skutterudites (13.1%), and half-Heuslers (8.4%), as shown in Fig. 8(c). It is worth pointing out that the peak *ZT* of our segmented leg is only ~1.1 at 125 ^{o}C, while PbTe:La and filled skutterudites have much higher *ZT* values of ~1.6 at 500 ^{o}C[43] and ~1.7 at 580 ^{o}C[45], respectively. Our study further demonstrates that achieving a high *ZT* across the entire temperature range is as important for efficiency as achieving a high peak *ZT*. Since thermoelectric devices must contain both n-type and p-type legs, a p-type leg with comparable efficiency is needed in order to achieve a device efficiency of 12.5%. Exploring the corresponding p-type (Bi, Sb)$_2$(Te, Se, S)$_3$-based legs could result in a lead-free substitute for p-type PbTe-based materials.[46-48]

Our study already clearly shows the promise to replace some toxic lead-containing materials by Bi_2Te_3-Bi_2Se_3-Bi_2S_3 based materials for medium temperature applications. However, it is worth pointing out that the metallization and thermal stability of these compositions need to be investigated before real industrial application consideration. Although the repeatedly measurement of the same sample shows good thermal stability for all the samples, the long-time thermal stability especially under a large temperature gradient has to be to studied.

4. Conclusions

A systematic study has been conducted on the Bi_2Te_3-Bi_2Se_3-Bi_2S_3 system. Bi_2Te_3 has the highest weighted mobility among all compositions, which corresponds to a high power factor. The lattice thermal conductivity map shows a minimum near $Bi_2Te_{1.2}Se_{1.8}$, owing to the strong alloy scattering to the phonon transport. The peak *ZT* of the classic n-type composition $Bi_2Te_{2.7}Se_{0.3}$ could be shifted from 125 to 275 ^{o}C by partially substituting Te with S. The temperature dependent *ZT* curve for $Bi_2Te_{2.3}Se_{0.3}S_{0.4}$ in the range from 200 to 325 ^{o}C is quite flat with an average value larger than 0.7. Additionally, two compounds, *i.e.*, $Bi_2Te_2S_1$ (*ZT* ~0.8 at 300 ^{o}C) and $Bi_2Se_1S_2$ (*ZT* ~0.8 at 500 ^{o}C), are promising for medium temperature power generation application. A segmented leg based on $Bi_2Te_{2.7}Se_{0.3}$ for 25-175 ^{o}C, $Bi_2Te_{2.5}Se_{0.3}S_{0.2}$ for 175-250 ^{o}C, $Bi_2Te_2S_1$ for 250-400 ^{o}C, and $Bi_2Se_1S_2$ for 400-500 ^{o}C has shown a leg efficiency of 12.5%

when the appropriate p-type leg is paired, which competes well with the state-of-the-art thermoelectric materials in the same temperature range, such as PbTe, PbSe, PbS, filled-skutterudite, and half Heusler, for application in solar thermal to electrical power generation.

References

1. J. R. Drabble and C. H. L. Goodman, J. Phys. Chem. Solid, 1958, 5, 142-144.
2. H. J. Goldsmid, J. Appl. Phys., 1961, 32, 2198-2202.
3. J. Jiang, L. D. Chen, S. Q. Bai, Q. Yao and Q. Wang, Scripta Mater., 2005, 52, 347-351.
4. X. B. Zhao, X. H. Ji, Y. H. Zhang, T. J. Zhu, J. P. Tu and X. B. Zhang, Appl. Phys. Lett., 2005, 86, 062111-03.
5. J. L. Cui, H. F. Xue, W. J. Xiu, L. Jiang and P. Z. Ying, J. Solid State Sci., 2006, 179, 3751-3755.
6. L. D. Zhao, B. P. Zhang, J. F. Li, H. L. Zhang and W. S. Liu, Solid State Sci., 2008, 10, 651-658.
7. B. Poudel, Q. Hao, Y. Ma, Y. C. Lan, A. Minnich, B. Yu, X. Yan, D. Z. Wang, A. Muto, D. Vashaee, X. Y. Chen, J. M. Liu, M. S. Dresselhaus, G. Chen and Z. F. Ren, Science, 2008, 320, 634-638.
8. Y. Ma, Q. Hao, B. Poudel, Y. C. Lan, B. Yu, D. Z. Wang, G. Chen and Z. F. Ren, Nano Lett., 2008, 8, 2580-2584.
9. L. D. Zhao, B. P. Zhang, W. S. Liu and J. F. Li, J. Appl. Phys., 2009, 105, 023704-6.
10. W. J. Xie, J. He, H. J. Kang, X. F. Tang, S. Zhu, M. Laver, S. Y. Wang, J. R. D. Copley, C. M. Brown, Q. J. Zhang and T. M. Tritt, Nano Lett., 2010, 10, 3283-3289.
11. X. Yan, B. Poudel, Y. Ma, W. S. Liu, G. Joshi, H. Wang, Y. C. Lan, D. Z. Wang, G. Chen and Z. F. Ren, Nano Lett., 2010, 10, 3373-3378.
12. W. S. Liu, Q. Y. Zhang, Y. C. Lan, S. Chen, X. Yan, Q. Zhang, H. Wang, D. Z. Wang, G. Chen and Z. F. Ren, Adv. Energy Mater., 2011, 1, 577-587.
13. K. McEnaney, D. Kraemer, Z. F. Ren and G. Chen, J Appl. Phys., 2011, 110, 074502-6.
14. D. Kraemer, B. Poudel, H. P. Feng, J. C. Caylor, B. Yu, X. Yan, Y. Ma, X. W. Wang, D. Z. Wang, A. Muto, K. McEnaney, M. Chiesa, Z. F. Ren and G. Chen, Nat. Mater., 2012, 10, 532-538.
15. N. K. Stark, T. E. Svechnikov and S. N. Chizhevskaya, Inorganic Mater., 1985, 21, 328-331.
16. H. Sherrer and S. Scherrer, Bismuth telluride, antimony telluride, and their solid solutions, in CRC Thermoelectric Handbook, edited by Rowe, D. M., CRC Press, Boca Raton, 1995.
17. T. S. Oh, D. B. Hyun and N. V. Kolomoets, Scripta Mater., 2000, 42, 849-854.
18. L. V. Prokofieva, D. A. Pshenay-Severin, P. P. Konstantinov and A. A. Shabaldin, Semiconductors, 2009, 43, 937-976.
19. A. Saji, S. Ampili, S. H. Yang, K. J. Ku and M. Elizabeth, J. Phys: Condens. Mater., 2005, 17, 2873-2888.
20. L. D. Zhao, B. P. Zhang, W. S. Liu, H. L. Zhang and J. F. Li, J. Solid State Chem., 2008, 181, 3278-3282.
21. Z. H. Ge, B. P. Zhang, Z. X. Yu and J. F. Li, J. Mater. Res., 2011, 26, 2711-2718.
22. Z. H. Ge, B. P. Zhang, Y. Liu and J. F. Li, Phys. Chem. Chem. Phys., 2012, 14, 4475-4481.
23. K. Biswas, L. D. Zhao and M. G. Kanatzidis, Adv. Energy Mater., 2012, 2, 634-638.
24. N. J. Cook, C. L. Ciobanu, T. Wagner and C. J. Stanley, Can. Mineral., 2007, 45, 665-708.
25. H. F. Liu, C. R. Knowles and L. L. Y. Chang, Can. Mineral., 1995, 33, 115-128.
26. J. F. Li, W. S. Liu, L. D. Zhao and M. Zhou, NPG Asia Mater., 2010, 2, 152-158.
27. W. S. Liu, X. Yan, G. Chen and Z. F. Ren, Nano Energy, 2012, 1, 42-56.
28. J. Horák, J. Navrátil and Z. Starý, J. Phys. Chem. Solids, 1992, 53,1067-1072.
29. J. Callaway, and H. C. von Baeyer, Phys. Rev. 1960, 120, 1149-1154.
30. B. Abeles, Phys. Rev. 1963, 131, 1906-1911.
31. W. Wong-Ng, H. Joress, J. Martin, P. Y. Zavalij, Y. Yan and J. Yang, Appl. Phys. Lett., 2012, 100, 082107-5.
32. H. J. Goldsmid, Electronic Refrigeration, Pion Ltd., London, 1986.
33. G. D. Mahan, J. Appl. Phys., 1989, 65, 1578-1583.
34. G. A. Slack, New materials and performance limits for thermoelectric cooling, in CRC Thermoelectric Handbook, edited by Rowe, D. M., CRC Press, Boca Raton, 1995.
35. W. S. Liu, B. P. Zhang, L. D. Zhao and J. F. Li, Chem. Mater., 2008, 20, 7526-7531.
36. W. S. Liu, B. P. Zhang, J. F. Li, H. L. Zhang and L. D. Zhao, J. Appl. Phys., 2007, 102, 103717-7.
37. J. M. Schultz, J. P. McHugh and W. A. Tiller, J. Appl. Phys., 1962, 33, 2443-2450.
38. H. J. Goldsmid, Introduction to thermoelectricity, Springer-Verlag, Berlin Heidelberg, 2010.
39. L. D. Zhao, S. H. Lo, J. Q. He, H. Li, K. Biswas, J. Androulakis, C. I. Wu, T. P. Hogan, D. Y. Chung, V. P. Dravid and M. G. Kanatzidis, J. Am. Chem. Soc., 2011, 133, 20476-20487.
40. G. Joshi, X. Yan, H. Z. Wang, W. S. Liu, G. Chen and Z. F. Ren, Adv. Energy Mater., 2011, 1, 643-647.
41. G. J. Snyder and T. S. Ursell, Phys. Rev. Lett., 2003, 91, 148021-4.
42. G. D. Mahan, J. Appl. Phys., 1991, 70, 4551-4554.
43. Y. Z. Pei, J. Lensch-Falk, E. S. Toberer, D. L. Medlin and G. J. Snyder, Adv. Funct. Mater., 2011, 21, 241-249.
44. Q. Y. Zhang, H. Wang, W. S. Liu, H. Z. Wang, B. Yu, Q. Zhang, Z. T. Tian, G. Ni, S. Lee, K. Esfarjani, G. Chen and Z. F. Ren, Energy Environ. Sci. 2012, 5, 5246-5251.

45. X. Shi, J. Yang, J. R. Salvador, M. F. Chi, J. Y. Cho, H. Wang, S. Q. Bai, J. H. Yang, W. Q. Zhang and L. D. Chen, J. Am. Chem. Soc. 2011, 133, 7837-7846.
46. Y. Z. Pei, X. Y. Shi, A. LaLonde, H. Wang, L. D. Chen and G. J. Snyder, Nature, 2011, 473, 66-69.
47. Q. Zhang, F. Cao, W. S. Liu, K. Lukas, B. Yu, S. Chen, C. Opeil, D. Broido, G. Chen and Z. F. Ren, J. Am. Chem. Soc., 2012, 134, 10031-10038.
48. K. Biswas, J. Q. He, Q. C. Zhang, G. Y. Wang, C. Uher, V. P. Dravid and M. G. Kanatzidis, Nat. Chem., 2011, 3, 160-166.

5

Table 1. Volumetric density, crystalline structure, lattice parameters, and atomic sites of some compounds in the Bi_2Te_3-Bi_2Se_3-Bi_2S_3 system.

Compounds	Density	Structure	Lattice parameter		Atomic site					
			Rhombohedral phases							
	(g/cm^3)		axis	(Å)		Bi(1)	Te(1)	Te(2)		
Bi_2Te_3		$R\bar{3}m$	a	4.3856	x	0	0	0		
	7.75	No. 166	b	4.3856	y	0	0	0		
			c	30.503	z	0.4005	0.2097	0		
	(g/cm^3)		axis	(Å)		Bi(1)	Te(1)	Se(1)		
$Bi_2Te_2Se_1$		$R\bar{3}m$	a	4.3001	x	0	0	0		
	7.63	No. 166	b	4.3001	y	0	0	0		
			c	30.000	z	0.3920	0.2160	0		
	(g/cm^3)	$R\bar{3}m$	axis	(Å)		Bi(1)	Se(1)	Te(1)		
$Bi_2Te_1Se_2$		No. 166	a	4.2178	x	0	0	0		
	7.49		b	4.2178	y	0	0	0		
			c	29.458	z	0.3989	0.2120	0		
Bi_2Se_3	(g/cm^3)		axis	(Å)		Bi(1)	Se(1)	Te(1)		
		$R\bar{3}m$	a	4.1396	x	0	0	0		
	7.47	No. 166	b	4.1396	y	0	0	0		
			c	28.634	z	0.4012	0.2121	0		
	(g/cm^3)		axis	(Å)		Bi(1)	Se(1)	Te(1)		
$Bi_2Te_2S_1$		$R\bar{3}m$	a	4.2535	x	0	0	0		
	7.49	No. 166	b	4.2535	y	0	0	0		
			c	29.608	z	0.3928	0.2143	0		
			orthorhombic phases							
	(g/cm^3)		axis	(Å)		Bi(1)	Bi(2)	Se(1)	S(1)	Se(2)
$Bi_2Se_2S_1$		Pnma	a	11.66327	x	0.51805	0.6542	0.6239	0.7115	0.4252
	7.36	No.62	b	4.068393	y	0.25	0.75	0.75	0.25	0.75
			c	11.44897	z	0.1689	0.4643	0.0697	0.2978	0.3687
	(g/cm^3)		axis	(Å)		Bi(1)	Bi(2)	S(1)	Se(1)	S(2)
$Bi_2Se_1S_2$		Pnma	a	11.5044	x	0.5164	0.6587	0.6164	0.7288	0.4630
	7.05	No.62	b	4.0254	y	0.25	0.75	0.75	0.25	0.75
			c	11.2959	z	0.1712	0.4633	0.0532	0.2986	0.3816
	(g/cm^3)		axis	(Å)		Bi(1)	Bi(2)	S(1)	S(2)	S(3)
Bi_2S_3		Pnma	a	11.2867	x	0.5174	0.6592	0.6154	0.7148	0.4505
	6.73	No.62	b	3.9816	y	0.25	0.75	0.75	0.25	0.75
			c	11.1421	z	0.1727	0.4663	0.0576	0.3055	0.3609